Predicting sound absorption in additively manufactured microporous labyrinthine structures

K. C. Opiela [1], **T. G. Zieliński** [1], **K. Attenborough** [2]
[1] Polish Academy of Sciences, Institute of Fundamental Technological Research,
ul. Pawińskiego 5B, 02-106 Warsaw, Poland
e-mail: **kopiela@ippt.pan.pl** (K. C. Opiela)

[2] The Open University, School of Engineering and Innovation,
Milton Keynes MK7 6AA, UK

Abstract
Low-frequency sound absorption by thin rigid porous hard-backed layers is enhanced if the geometrical tortuosity is increased. Increasing tortuosity increases the fluid flow path length through the porous layer thereby increasing the effective thickness. In turn, this reduces the effective sound speed within the layer and the frequency of the quarter wavelength layer resonance. One way of increasing tortuosity is through rectangular labyrinthine channel perforations. In addition to the tortuosity of the porous matrix, the bulk tortuosity value is influenced by the channel widths, lengths, and number of folds. A sample with an impervious skeleton and a sample in which the solid skeleton is perforated with oblique cylindrical holes evenly spaced in a rectangular pattern have been fabricated using conventional methods and an additive manufacturing technology, respectively. The sound absorption spectra resulting from these structures have been predicted analytically as well as numerically and compared with normal incidence impedance-tube measurements.

1 Introduction

One of the methods of improving acoustic material properties by reducing quarter wavelength layer resonance frequencies is the increase of the structure's tortuosity, which is the squared ratio of the length of the actual path taken by the moving fluid to the distance between its ends. With a labyrinthine pore network, values of tortuosity greater than ten are easily achievable and lead to potentially useful narrowband deep sub-wavelength sound absorption peaks [1]. If the material skeleton is permeable to acoustic waves and its resistivity to air flow is sufficiently high, additional dissipative phenomena occur that originate from double-porosity and pressure diffusion effects [2]. Integrating influences of these two mechanisms with high tortuosity can make thin hard-backed porous layers very efficient in sound absorption.

Various labyrinthine-like solutions have been proposed so far. Recently, the concept of a labyrinthine structure combined with an acoustic foam has been studied in [3]. Significant enhancements in low-frequency sound absorption have been reported and confirmed experimentally over a homogeneous porous material under the same thickness. Some possible labyrinthine slit configurations oriented both vertically as well as horizontally have been investigated in [1, 4]. It is also where the double-porosity theory [2] has been used to calculate normal incidence sound absorption coefficient spectra resulting from labyrinthine structures with a microporous skeleton. Examples including microslit perforations are given therein to depict great benefits offered by highly tortuous, double-porosity materials with the pressure diffusion effect. However, previous research [5, 6, 7] shows that manufacturing of relatively narrow (e.g. 0.3 mm-wide) inclined slits in budget additive technologies is feasible albeit fraught with problems. Other primitive shapes, like cylindrical microchannels, seem to be more suitable for application in a labyrinthine slit sample intended for experimental verification of the developed formulae.

This contribution is a continuation of the work reported in the papers [1, 4, 5, 6, 7]. It concentrates on

predicting and measuring the normal incidence sound absorption in a three-dimensionally printed double-porosity labyrinthine structure. Its rigid skeleton is perforated using regular, straight, inclined cylindrical channels which makes it permeable to acoustic waves. For completeness, the modelling and experimental results obtained for a conventionally manufactured single-porosity material are also presented.

2 Labyrinthine geometry

Two microgeometries are proposed to investigate the sound absorption performance of solid and microporous rigid labyrinthine slit architectures:

1. a horizontal labyrinthine slit structure with an impervious skeleton (see Fig. 1);
2. a labyrinthine slit structure of the identical mesoscopic shape and dimensions as in 1 but with a regularly perforated and therefore permeable skeleton.

They were designed in such a way that their manufacturing is facilitated, and to achieve as large scale separation between layer and skeleton permeabilities in 2 as possible using budget fabrication methods. For this reason, a cylindrical perforation of diameter $d_{\text{perf}} = 0.4\,\text{mm}$, inclined at the angle $\vartheta_{\text{perf}} = 45°$ to the direction of incidence, and evenly spaced every $l_{\text{perf}} = 0.8\,\text{mm}$ (the distance between perforation axes) is assumed in 2. The slit width, $w_{\text{s}} = 3l_{\text{perf}}/\sin\vartheta_{\text{perf}} \approx 3.39\,\text{mm}$, and skeleton wall thickness, $w_{\text{w}} = 5l_{\text{perf}}/\sin\vartheta_{\text{perf}} \approx 5.66\,\text{mm}$, were selected in a manner that the perforation channels are straight

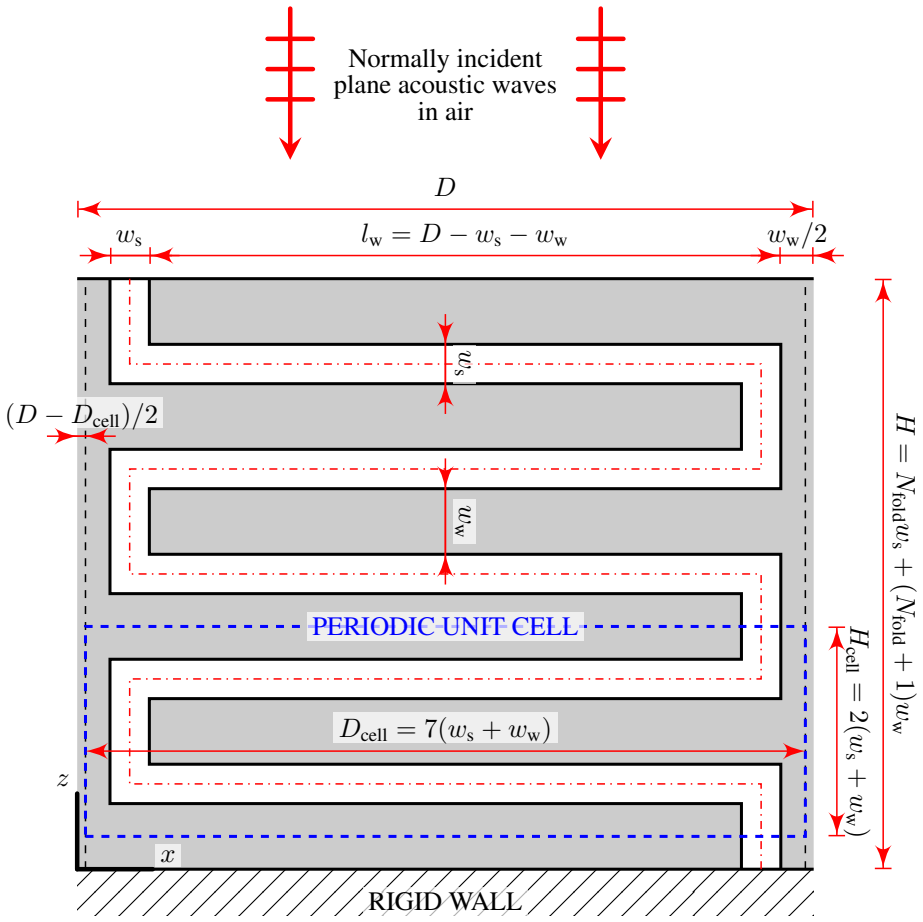

Figure 1: The cross-section of a single labyrinthine slit in a cylindrical sample of diameter D with a skeleton marked in grey. The geometrical parameters describing the layer and the boundaries of the representative periodic unit cell (blue dashed line) are shown. The slit centre line is represented by the dash-dotted red line.

and continuous in the whole material volume. The dimensions D_{cell} and H_{cell} of the periodic unit cells representative for the studied architectures are multiples of $w_{\text{s}} + w_{\text{w}}$ for the same reason. The samples were prepared to have a diameter of $D = 63.5\,\text{mm}$ to fit an impedance tube of this size. Considering one labyrinthine slit with $N_{\text{fold}} = 5$ folds in the sample, its thickness (i.e. layer thickness) and the length of horizontal skeleton wall fragments are $H = N_{\text{fold}} w_{\text{s}} + (N_{\text{fold}} + 1) w_{\text{w}} \approx 50.91\,\text{mm}$ and $l_{\text{w}} = D - w_{\text{s}} - w_{\text{w}} \approx 54.45\,\text{mm}$, respectively.

3 Modelling, manufacturing, and testing methods

3.1 Evaluation of the acoustic absorption coefficient

The normal incidence sound absorption coefficient, $\mathcal{A}(\omega)$, at temporal frequencies, f, from the range $[0\,\text{Hz}, 1\,\text{kHz}]$ is calculated as [8, 9]:

$$\mathcal{A}(\omega) = 1 - \left| \frac{Z_{\text{s}} - Z_{\text{air}}}{Z_{\text{s}} + Z_{\text{air}}} \right|^2 , \tag{1}$$

where $\omega = 2\pi f$ is the angular frequency,

$$Z_{\text{s}}(\omega) = -\text{i}\, Z_{\text{eq}} \cot\left(\omega H c_{\text{eff}}^{-1}\right) \tag{2}$$

is the surface acoustic impedance for a hard-backed porous layer of thickness H saturated with air (i is the imaginary unit), whereas $Z_{\text{air}} = \sqrt{\varrho_{\text{air}} K_{\text{air}}}$, $\varrho_{\text{air}} = 1.204\,\text{kg/m}^3$, and $K_{\text{air}} = 141855\,\text{Pa}$ denote the characteristic impedance, mass density and bulk modulus of air, respectively. Because the approach is based on replacing the porous layer by a fluid equivalent to it in macroscopic properties, one defines the so-called equivalent characteristic impedance, $Z_{\text{eq}}(\omega) = \sqrt{\varrho_{\text{eq}} K_{\text{eq}}}$, and the effective speed of sound, $c_{\text{eff}}(\omega) = \sqrt{K_{\text{eq}}/\varrho_{\text{eq}}}$, in the homogenised medium in terms of the equivalent density, $\varrho_{\text{eq}}(\omega)$, and equivalent bulk modulus, $K_{\text{eq}}(\omega)$. These latter two complex-valued functions are formulated by various models, in particular those presented below.

3.1.1 Modelling the material with impervious matrix

For simple microstructures, like labyrinthine slits, the properties of the equivalent fluid can be determined analytically. To evaluate the analytical ('A') equivalent density, $\varrho_{\text{eq}}^{\text{A}}(\omega)$, and bulk modulus, $K_{\text{eq}}^{\text{A}}(\omega)$, the knowledge about the open porosity, ϕ, and the analytical approximation of the kinematic tortuosity of the structure, α_∞^{A}, is required along with the Prandtl number, $N_{\text{Pr,air}} = 0.71$, the dynamic viscosity, $\mu_{\text{air}} = 18.27 \cdot 10^{-6}\,\text{Pa} \cdot \text{s}$, and other properties of air [10, 11]:

$$\varrho_{\text{eq}}^{\text{A}}(\omega) = \frac{\varrho_{\text{air}}}{\phi} \alpha_\infty^{\text{A}} \left(1 - \frac{\tanh\chi}{\chi}\right)^{-1}, \qquad \chi(\omega) = \frac{w_{\text{s}}}{2} \sqrt{\text{i}\omega \frac{\varrho_{\text{air}}}{\mu_{\text{air}}}}\,, \tag{3}$$

$$K_{\text{eq}}^{\text{A}}(\omega) = \frac{K_{\text{air}}}{\phi} \left(\gamma_{\text{air}} - (\gamma_{\text{air}} - 1)\left(1 - \frac{\tanh\chi'}{\chi'}\right)\right)^{-1}, \qquad \chi'(\omega) = \frac{w_{\text{s}}}{2} \sqrt{\text{i}\omega \frac{N_{\text{Pr,air}} \varrho_{\text{air}}}{\mu_{\text{air}}}}\,, \tag{4}$$

where $\gamma_{\text{air}} = 1.4$ is the ratio of specific heats (the adiabatic index) for air. The open porosity is deduced directly from the microgeometry and takes the form:

$$\phi = \frac{w_{\text{s}}(w_{\text{s}} + w_{\text{w}} + l_{\text{w}})}{D_{\text{cell}}(w_{\text{s}} + w_{\text{w}})} = \frac{w_{\text{s}}(w_{\text{s}} + w_{\text{w}} + l_{\text{w}})}{7(w_{\text{s}} + w_{\text{w}})^2}\,. \tag{5}$$

The analytical kinematic tortuosity, on the other hand, is calculated as the squared ratio between the length of path along labyrinthine slit centre line (see Fig. 1) and the material layer thickness [1]:

$$\alpha_\infty^{\text{A}} = \left(\frac{N_{\text{fold}} w_{\text{s}} + (N_{\text{fold}} + 1) w_{\text{w}} + N_{\text{fold}} l_{\text{w}}}{N_{\text{fold}} w_{\text{s}} + (N_{\text{fold}} + 1) w_{\text{w}}}\right)^2 = \left(1 + \frac{N_{\text{fold}} l_{\text{w}}}{H}\right)^2 . \tag{6}$$

Alternatively, the equivalent density and bulk modulus of a rigid-frame porous material can be expressed according to the Johnson-Champoux-Allard-Lafarge (JCAL) model [12, 13, 14, 15] as:

$$\varrho_{\mathrm{eq}}^{\mathrm{N}}(\omega) = \frac{\varrho_{\mathrm{air}}}{\phi}\left(\alpha_{\infty}^{\mathrm{N}} + \frac{1}{\mathrm{i}\omega}\frac{\mu_{\mathrm{air}}}{\varrho_{\mathrm{air}}}\frac{\phi}{k_0^{\mathrm{N}}}\sqrt{\mathrm{i}\omega\frac{\varrho_{\mathrm{air}}}{\mu_{\mathrm{air}}}\left(\frac{2\alpha_{\infty}^{\mathrm{N}}k_0^{\mathrm{N}}}{\Lambda\phi}\right)^2 + 1}\right), \tag{7}$$

$$K_{\mathrm{eq}}^{\mathrm{N}}(\omega) = \frac{K_{\mathrm{air}}}{\phi}\left(\gamma_{\mathrm{air}} - (\gamma_{\mathrm{air}}-1)\left(1 + \frac{1}{\mathrm{i}\omega}\frac{\mu_{\mathrm{air}}}{N_{\mathrm{Pr,air}}\varrho_{\mathrm{air}}}\frac{\phi}{k_0'}\sqrt{\mathrm{i}\omega\frac{N_{\mathrm{Pr,air}}\varrho_{\mathrm{air}}}{\mu_{\mathrm{air}}}\left(\frac{2k_0'}{\Lambda'\phi}\right)^2 + 1}\right)^{-1}\right)^{-1}. \tag{8}$$

In this approach the six necessary geometrical parameters—the open porosity, ϕ, static viscous permeability, k_0^{N}, static thermal permeability, k_0', kinematic tortuosity, $\alpha_{\infty}^{\mathrm{N}}$, viscous characteristic length, Λ, and thermal characteristic length, Λ'—are estimated numerically on a unit cell geometry (see Fig. 1) using finite-element solutions to three steady boundary-value problems (hence the superscript 'N'). For more information, see e.g. [7, 9].

3.1.2 Modelling the material with permeable matrix

Because of the regularity and simplicity of the designed perforation, the material composed of the main labyrinthine slit surrounded by the permeable skeleton can be homogenised and virtually replaced by an equivalent fluid too. Its acoustically relevant equivalent properties—density, $\varrho_{\mathrm{eq}}^{\mathrm{N,DP}}(\omega)$, and bulk modulus, $K_{\mathrm{eq}}^{\mathrm{A,DP}}(\omega)$—are evaluated using the double-porosity ('DP') theory [2]:

$$\varrho_{\mathrm{eq}}^{\mathrm{N,DP}}(\omega) = \frac{\varrho_{\mathrm{air}}}{\phi^{\mathrm{DP}}}\left(\alpha_{\infty}^{\mathrm{N,DP}} + \frac{1}{\mathrm{i}\omega}\frac{\mu_{\mathrm{air}}}{\varrho_{\mathrm{air}}}\frac{\phi^{\mathrm{DP}}}{k_0^{\mathrm{N,DP}}}\sqrt{\mathrm{i}\omega\frac{\varrho_{\mathrm{air}}}{\mu_{\mathrm{air}}}\left(\frac{2\alpha_{\infty}^{\mathrm{N,DP}}k_0^{\mathrm{N,DP}}}{\Lambda^{\mathrm{DP}}\phi^{\mathrm{DP}}}\right)^2 + 1}\right), \tag{9}$$

$$K_{\mathrm{eq}}^{\mathrm{A,DP}}(\omega) = \left(\frac{1}{K_{\mathrm{eq}}^{\mathrm{A}}} + \frac{(1-\phi)F_{\mathrm{d}}}{K_{\mathrm{eq}}^{\mathrm{A,m}}}\right)^{-1}, \tag{10}$$

where $K_{\mathrm{eq}}^{\mathrm{A,m}}(\omega)$ is the complex, analytical equivalent bulk modulus for the microporous skeleton (superscript 'm') given by [10]:

$$K_{\mathrm{eq}}^{\mathrm{A,m}}(\omega) = \frac{K_{\mathrm{air}}}{\phi^{\mathrm{m}}}\left(\gamma_{\mathrm{air}} - (\gamma_{\mathrm{air}}-1)G\left(\frac{d_{\mathrm{perf}}}{2}\sqrt{-\mathrm{i}\omega\frac{N_{\mathrm{Pr,air}}\varrho_{\mathrm{air}}}{\mu_{\mathrm{air}}}}\right)\right)^{-1}. \tag{11}$$

In the above formulae, the open porosity of the microperforation is:

$$\phi^{\mathrm{m}} = \frac{1}{4}\pi\left(\frac{d_{\mathrm{perf}}}{l_{\mathrm{perf}}}\right)^2, \tag{12}$$

the total open porosity of the microporous architecture is:

$$\phi^{\mathrm{DP}} = \phi + (1-\phi)\phi^{\mathrm{m}}, \tag{13}$$

and $G(\xi) = 1 - 2J_1/(\xi J_0)$, where $J_0(\xi)$ and $J_1(\xi)$ are the Bessel functions of the first kind of zero and first order, respectively. The function $\varrho_{\mathrm{eq}}^{\mathrm{N,DP}}(\omega)$ is approximated by the JCAL model with the unknown numerical parameters $\alpha_{\infty}^{\mathrm{N,DP}}$, $k_0^{\mathrm{N,DP}}$, and Λ^{DP} computed on a microporous unit cell geometry by conducting two static analyses [7, 9]. It should be noted that the formula (9) is appropriate only for materials with low permeability contrast. In general, it is estimated numerically from harmonic flow problems [2]. In addition to the modified overall visco-inertial and thermal losses due to the presence of $\varrho_{\mathrm{eq}}^{\mathrm{N,DP}}(\omega)$ and $K_{\mathrm{eq}}^{\mathrm{A,m}}(\omega)$, extra dissipation effects are accounted for in the pressure ratio function, $F_{\mathrm{d}}(\omega)$, provided that there is a high permeability contrast between the pores at micro- and mesoscale levels. The function $F_{\mathrm{d}}(\omega)$ describes the ratio between the average pressure in the microporous domain and the pressure in the main pore network,

and is defined as follows [2]:

$$F_{\mathrm{d}}(\omega) = 1 - \mathrm{i}\frac{k_{\mathrm{d}}}{k_{\mathrm{d}}(0)}\frac{\omega}{\omega_{\mathrm{d}}}\,, \tag{14}$$

where the dynamic pressure diffusion, $k_{\mathrm{d}}(\omega)$, and the corresponding characteristic frequency, ω_{d}, are calculated for the studied material as:

$$k_{\mathrm{d}}(\omega) = \frac{1}{\mathrm{i}\omega}(1-\phi)\nu_{\mathrm{d}}\Big(1 - \frac{\tanh\chi_{\mathrm{d}}}{\chi_{\mathrm{d}}}\Big)\,, \qquad \chi_{\mathrm{d}}(\omega) = \frac{\Lambda_{\mathrm{d}}}{2}\sqrt{\mathrm{i}\omega\frac{1}{\nu_{\mathrm{d}}}}\,, \tag{15}$$

$$\omega_{\mathrm{d}} = (1-\phi)\frac{\nu_{\mathrm{d}}}{k_{\mathrm{d}}(0)}\,. \tag{16}$$

Here, the characteristic length for the pressure diffusion effects reads:

$$\Lambda_{\mathrm{d}} = \frac{7(w_{\mathrm{s}}+w_{\mathrm{w}})^2 - w_{\mathrm{s}}(w_{\mathrm{s}}+w_{\mathrm{w}}+l_{\mathrm{w}})}{w_{\mathrm{s}}+w_{\mathrm{w}}+l_{\mathrm{w}}} = \frac{7(w_{\mathrm{s}}+w_{\mathrm{w}})^2}{w_{\mathrm{s}}+w_{\mathrm{w}}+l_{\mathrm{w}}} - w_{\mathrm{s}} \tag{17}$$

and constitutes the doubled ratio between the volume of the microporous domain and the area of the interface between it and the main pore network.

$$\nu_{\mathrm{d}} = \frac{K_{\mathrm{air}}k_0^{\mathrm{A,m}}}{\phi^{\mathrm{m}}\gamma_{\mathrm{air}}\mu_{\mathrm{air}}} \tag{18}$$

is the pressure diffusivity of the microporous material. Inserting (15) and (16) to (14) simplifies the formula for the pressure ratio function:

$$F_{\mathrm{d}}(\omega) = \frac{\tanh\chi_{\mathrm{d}}}{\chi_{\mathrm{d}}}\,. \tag{19}$$

If the permeability contrast is sufficient, $\varrho_{\mathrm{eq}}^{\mathrm{N,DP}}(\omega) \approx \varrho_{\mathrm{eq}}^{\mathrm{N}}(\omega)$ and the pressure diffusion phenomenon giving rise to a low-frequency peak in the absorption spectrum is predicted. The analytical static viscous permeability, $k_0^{\mathrm{A,m}}$, for cylindrical micropores is determined from the Kozeny-Carman relationship [10, 16]:

$$k_0^{\mathrm{A,m}} = \frac{1}{32}\phi^{\mathrm{m}}d_{\mathrm{perf}}^2\cos^2\vartheta_{\mathrm{perf}}\,. \tag{20}$$

3.2 Preparation of cylindrical material samples

Two manufacturing techniques were used to fabricate cylindrical specimens of diameter $D = 63.5\,\mathrm{mm}$ and thickness $H \approx 50.9\,\mathrm{mm}$ of each considered material, shown in Fig. 2. The first impervious labyrinthine configuration was prepared conventionally by turning and milling from Nylon 6; see Fig. 2a. The second sample (see Fig. 2b) was three-dimensionally printed from a low-viscosity photocurable resin in the photopolymerisation technique exploiting a liquid–crystal display. The device used was Zortrax Inkspire with the component layer thickness equal $0.025\,\mathrm{mm}$. The sample was washed in an isopropyl alcohol to clean it from resin residue after removal from the printer. To facilitate the production process, both structures were not manufactured in one piece, but were assembled from six L-shaped elements instead.

3.3 Impedance tube measurements

The two-microphone transfer function method [17] was used to determine normal incidence sound absorption coefficient from acoustic pressure measurements performed on the samples in the 63.5-mm Brüel & Kjær Type 4206 circular impedance tube. During the tests the specimens fitted well into the tube and were backed by a rigid impervious piston. Previous comparative research [18] shows that the operation of the equipment is correct.

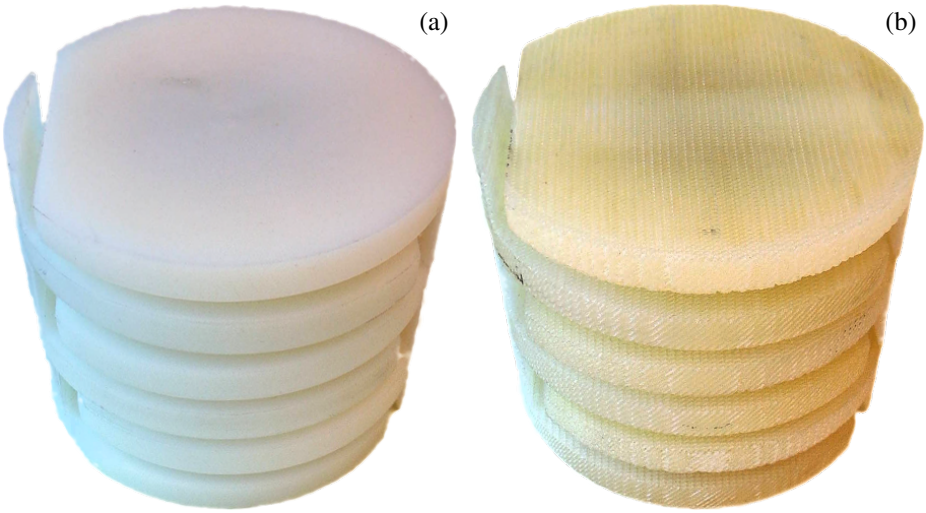

Figure 2: Photographs of (a) conventionally and (b) additively manufactured cylindrical material samples: the labyrinthine sample with (a) an impervious skeleton; (b) a permeable matrix due to the regular cylindrical perforation applied to the solid skeleton.

4 Results

The values of the sound absorption coefficient at normal incidence for the single-porosity labyrinthine material were predicted analytically as well as numerically and juxtaposed with experimental data obtained for the cylindrical sample. The results are plotted versus frequency in Fig. 3. They suggest that the calculated analytical kinematic tortuosity value, $\alpha_\infty^{\mathrm{A}} \approx 40.29$, is understated as the predicted frequency of the first

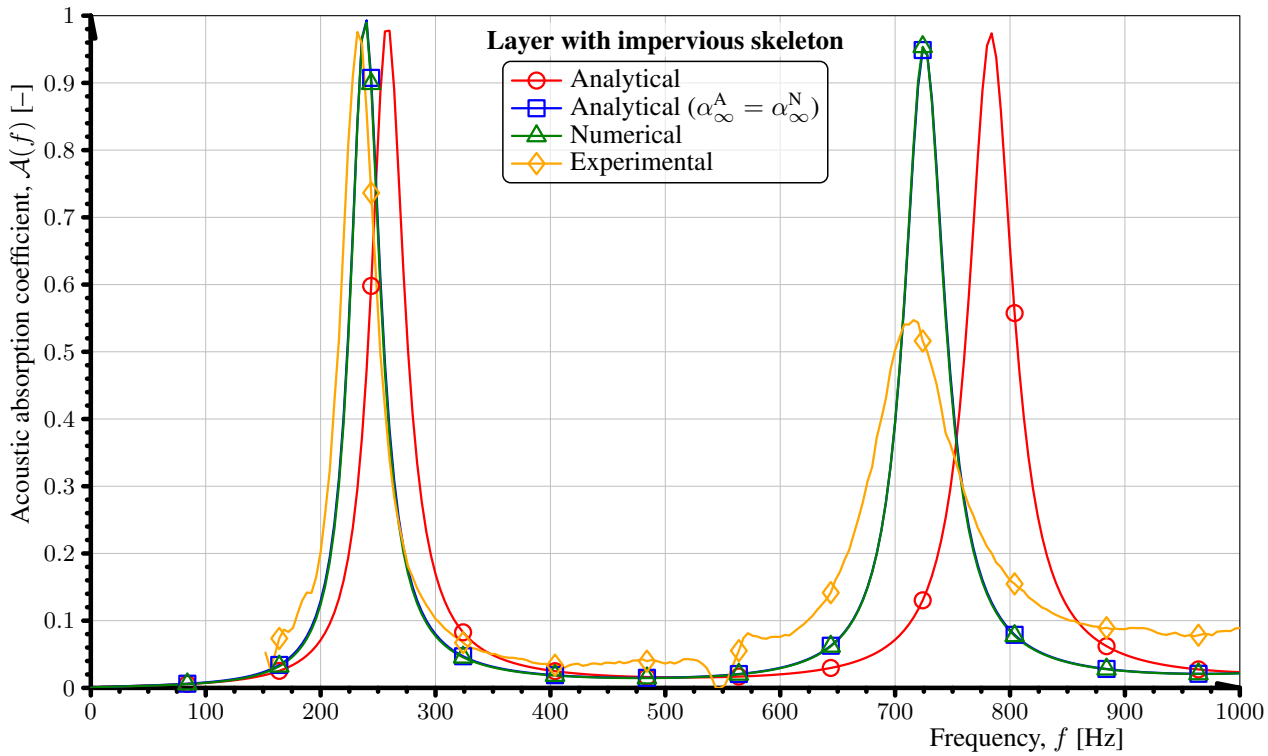

Figure 3: Measured and predicted (analytically and numerically) normal incidence sound absorption coefficient spectra for a 50.9 mm-thick hard-backed labyrinthine layer with an impervious skeleton ($w_{\mathrm{s}} \approx 3.4$ mm, $w_{\mathrm{w}} \approx 5.7$ mm, $l_{\mathrm{w}} \approx 54.4$ mm, $N_{\mathrm{fold}} = 5$).

quarter wavelength layer resonance is higher than measured in the impedance tube. Typically, the higher the value of tortuosity of a porous network, the lower the first quarter wavelength layer resonance frequency. To investigate it further, a two-dimensional numerical analysis incorporating the finite element method [19] was conducted. Open-source pre-processing software was used to prepare the CAD model of the periodic air region in the $D_{\text{cell}} \times H_{\text{cell}}$ unit cell (see Fig. 1) and discretise the corresponding domain. The computations with $415\,847$ and $937\,747$ degrees of freedom were run in the FEniCS library [20] distributed under the GNU Lesser General Public License. The six evaluated JCAL parameters are listed in Tab. 1. Good qualitative and quantitative agreement is reached between the numerical and experimental curves (see Fig. 3). Nevertheless, the magnitude of the second absorption peak around $725\,\text{Hz}$ is vastly overpredicted, which seems to be the result of sample geometrical imperfections (the numerical model is idealised). However, practically the same modelling result is achieved if α_∞^{A} in the analytical approach is replaced by $\alpha_\infty^{\text{N}} \approx 46.9 > \alpha_\infty^{\text{A}}$. This proves that the analytical kinematic tortuosity evaluation based on the slit centre line length is imprecise, which is probably due to the relatively large slit width w_{s}. All in all, the experimental data shows that the proposed labyrinthine structure is efficient in dissipating acoustic wave energy at comparatively low frequencies, providing nearly perfect albeit narrow sound absorption at $235\,\text{Hz}$.

Table 1: The numerical JCAL parameters for the impervious labyrinthine structure.

Parameter	Symbol	Unit	Value
Open porosity	ϕ	–	0.376
Static viscous permeability	k_0^{N}	$10^{-9}\,\text{m}^2$	7.52
Static thermal permeability	k_0'	$10^{-9}\,\text{m}^2$	369.2
Kinematic tortuosity	α_∞^{N}	–	46.9
Viscous characteristic length	Λ	mm	3.25
Thermal characteristic length	Λ'	mm	3.39

Fig. 4 illustrates the calculation and measurement results pertaining to the labyrinthine slit material with the microperforated skeleton of microporosity $\phi^{\text{m}} \approx 0.196$. The total porosity of the configuration is $\phi^{\text{DP}} \approx 0.496$. The numerical analyses with periodic as well as symmetric boundary conditions contained $1\,204\,592$ and $3\,833\,121$ degrees of freedom and were run on a three-dimensional unit cell of dimensions $D_{\text{cell}} \times H_{\text{cell}} \times l_{\text{perf}}/2$ representative for the microporous architecture. The reference analytical black curve is plotted to visualise the advantage coming from the double-porosity effect over the uniform single-porosity configuration with cylindrical channels inclined at $45°$ to the insonified surface. The experimental sound absorption for the studied microporous structure is more broadband than it is for the single-porosity labyrinthine case (cf. Fig. 3), and its first peak is lowered to $650\,\text{Hz}$ from $950\,\text{Hz}$ predicted for the single-porosity perforated layer. The separation of permeability scales is poor since $k_0^{\text{N}}/k_0^{\text{A,m}} \approx 15$ and thus the pressure diffusion phenomenon is weak. In consequence, the imaginary part of the pressure ratio function, $\mathbb{I}\text{m}\, F_{\text{d}}(\omega)$, is close to zero in the considered frequency range, which means that the pressure diffusion mechanism does not contribute to the overall sound absorption. The agreement between double-porosity predictions and measurements is not satisfactory. The estimated frequency of the first absorption peak is higher by about $300\,\text{Hz}$ than the experimental value. Additionally, the predicted absorption coefficient reaches 0.95 in the peak, whereas the measurement reveals maximal absorption of about 0.75. The discrepancies are to some extent attributed to the quality of the sample, which is quite complicated geometrically from the point of view of budget additive manufacturing. Because of the channel diameters being at the limit of fabrication, and the correlation between the printing direction and gravity, the microperforation obtained is not as uniform as the one in modelling. However, more research is needed to find the real cause of the observed disagreement.

5 Conclusions

The following conclusions from the research are drawn:

- Labyrinthine structures are potentially useful low-frequency narrow-band sound absorbers due to their extraordinary high tortuosity values.

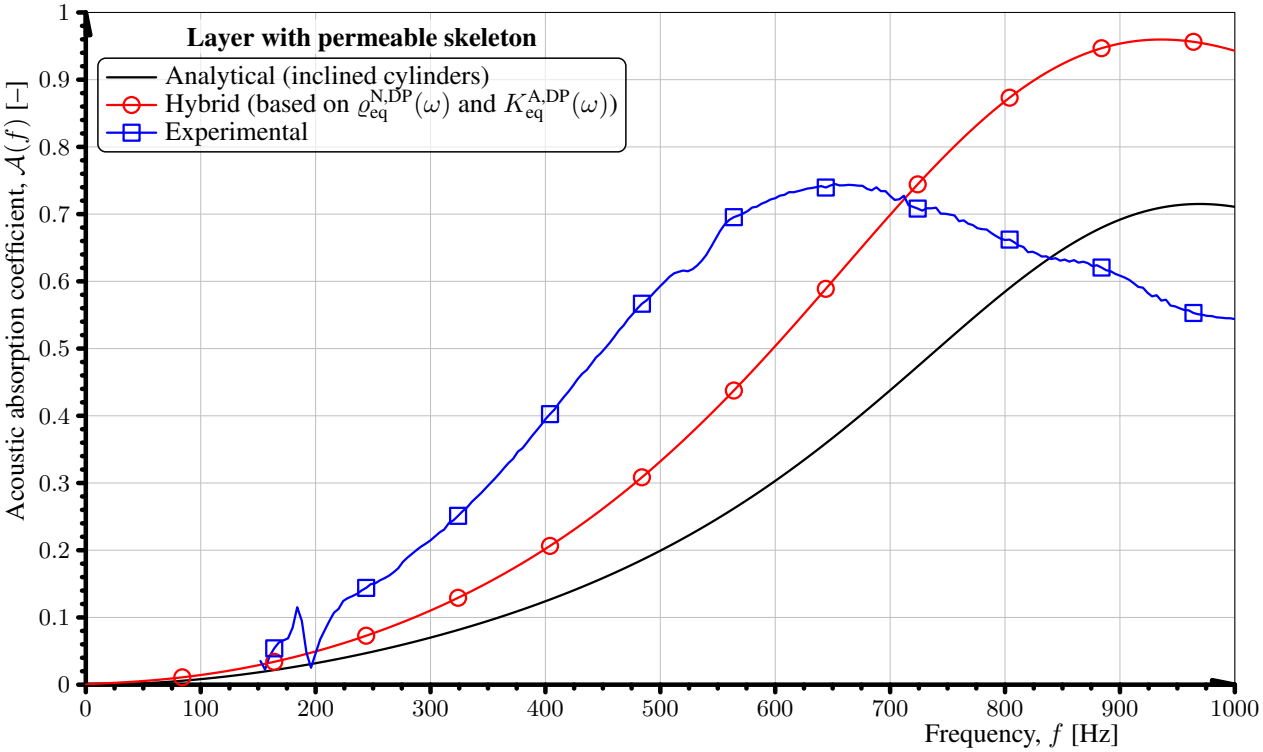

Figure 4: Measured and predicted normal incidence sound absorption coefficient spectra for a 50.9 mm-thick hard-backed layer of identical 3.4 mm-wide labyrinthine slits separated by 5.7 mm-thick permeable walls with $l_{\mathrm{w}} \approx 54.4$ mm and $N_{\mathrm{fold}} = 5$. The micropores of the skeleton have the form of cylindrical channels of diameter 0.4 mm inclined at 45° to the wave propagation direction and regularly spaced every 0.8 mm. The analytical result for a 50.9 mm-thick hard-backed single-porosity layer composed of inclined cylindrical channels (black line) is given for comparison.

- Good agreement between the calculations and measurements is found for the labyrinthine slit configuration with an impervious matrix.
- The analytically evaluated tortuosity based on the length of labyrinthine channel centre line is lower than its numerical analogue, and the difference is central to precise modelling.
- The combined influence of the labyrinthine slit tortuosity and the double-porosity effect makes the acoustic absorption in the structure more broadband at frequencies around 650 Hz.
- The performance of the absorber is supposed to enhance if the permeability contrast between its meso- and micropore networks is increased.
- Insufficient quality of the sample is to some extent responsible for significant discrepancies between modelling and experimental results for the double-porosity case.
- The agreement between predictions and measurements is expected to improve if a cuboidal sample is prepared (instead of the cylindrical one) and tested in an impedance tube with square cross-section.

Further work focused mainly on the preparation of a new high-quality sample with permeable skeleton is needed to investigate the reason for the reported inaccuracies in the obtained hybrid double-porosity predictions. Another modelling approaches based more on numerical solutions are also planned.

Acknowledgements

The financial support of the projects number 2020/37/N/ST8/04071: “Impact of the 3D printing process on the acoustic properties of porous materials”, and 2021/41/B/ST8/04492: “Sound-absorbing composites:

coupled acoustic energy dissipation mechanisms, multiscale modelling and prototyping", financed by the National Science Centre (NCN), Poland, is gratefully acknowledged.

References

[1] K. Attenborough, "Analytical approximations for sub wavelength sound absorption by porous layers with labyrinthine slit perforations," *Applied Sciences*, vol. 11, no. 8, pp. 1–10, article 3299, Apr. 2021.

[2] X. Olny and C. Boutin, "Acoustic wave propagation in double porosity media," *Journal of the Acoustical Society of America*, vol. 114, no. 1, p. 73, Jul. 2003.

[3] H. Zhao, Y. Wang, D. Yu, H. Yang, J. Zhong, F. Wu, and J. Wen, "A double porosity material for low frequency sound absorption," *Composite Structures*, vol. 239, pp. 1–6, article 111 978, May 2020.

[4] K. Attenborough, "Analytical approximations for sound absorption by labyrinthine architectures," in *SAPEM2020+1 — 6th Symp. on the Acoustics of Poro-Elastic Materials*. West Lafayette, USA: Purdue University, Apr. 2021.

[5] K. C. Opiela, T. G. Zieliński, and K. Attenborough, "Manufacturing, modeling, and experimental verification of slitted sound absorbers," in *Proc. of ISMA2020 International Conference on Noise and Vibration Engineering/USD2020 International Conference on Uncertainty in Structural Dynamics*, W. Desmet, B. Pluymers, D. Moens, and S. Vandemaele, Eds. Heverlee, Belgium: Katholieke Universiteit Leuven, Department of Mechanical Engineering, Sep. 2020, pp. 409–420.

[6] K. C. Opiela, T. G. Zieliński, and K. Attenborough, "Impedance-tube characterisation of additively manufactured slitted sound absorbers," in *SAPEM2020+1 — 6th Symp. on the Acoustics of Poro-Elastic Materials*. West Lafayette, USA: Purdue University, Apr. 2021.

[7] K. C. Opiela, T. G. Zieliński, and K. Attenborough, "Limitations on validating slitted sound absorber designs through budget additive manufacturing," *Materials & Design*, vol. 218, pp. 1–17, article 110 703, Jun. 2022.

[8] J.-F. Allard and N. Atalla, *Propagation of sound in porous media: Modelling sound absorbing materials*, 2nd ed. John Wiley & Sons, Oct. 2009.

[9] T. G. Zieliński, R. Venegas, C. Perrot, M. Červenka, F. Chevillotte, and K. Attenborough, "Benchmarks for microstructure-based modelling of sound absorbing rigid-frame porous media," *Journal of Sound and Vibration*, vol. 483, pp. 1–38, article 115 441, Sep. 2020.

[10] K. Attenborough, "Microstructures for lowering the quarter wavelength resonance frequency of a hard-backed rigid-porous layer," *Applied Acoustics*, vol. 130, pp. 188–194, Jan. 2018.

[11] K. Attenborough, "Macro- and micro-structure designs for porous sound absorbers," *Applied Acoustics*, vol. 145, pp. 349–357, Feb. 2019.

[12] D. L. Johnson, J. Koplik, and R. Dashen, "Theory of dynamic permeability and tortuosity in fluid-saturated porous media," *Journal of Fluid Mechanics*, vol. 176, pp. 379–402, Mar. 1987.

[13] Y. Champoux and J.-F. Allard, "Dynamic tortuosity and bulk modulus in air-saturated porous media," *Journal of Applied Physics*, vol. 70, no. 4, pp. 1975–1979, Aug. 1991.

[14] D. Lafarge, "Comments on "Rigorous link between fluid permeability, electric conductivity, and relaxation times for transport in porous media"," *Physics of Fluids A: Fluid Dynamics*, vol. 5, no. 2, pp. 500–502, Feb. 1993.

[15] D. Lafarge, P. Lemarinier, J.-F. Allard, and V. Tarnow, "Dynamic compressibility of air in porous structures at audible frequencies," *Journal of the Acoustical Society of America*, vol. 102, no. 4, pp. 1995–2006, Oct. 1997.

[16] P. C. Carman, *Flow of gases through porous media*. London: Butterworths Scientific Publications, 1956.

[17] ISO 10534-2, "Acoustics — Determination of sound absorption coefficient and impedance in impedance tubes — Part 2: Transfer-function method," International Organisation for Standardization, Case postale 56, CH-1211 Genève 20, Switzerland, ISO standard, Nov. 1998.

[18] T. G. Zieliński, K. C. Opiela, P. Pawłowski, N. Dauchez, T. Boutin, J. Kennedy, D. Trimble, H. Rice, B. Van Damme, G. Hannema, R. Wróbel, S. Kim, S. Ghaffari Mosanenzadeh, N. X. Fang, J. Yang, B. Briere de la Hosseraye, M. C. J. Hornikx, E. Salze, M.-A. Galland, R. Boonen, A. Carvalho de Sousa, E. Deckers, M. Gaborit, and J.-P. Groby, "Reproducibility of sound-absorbing periodic porous materials using additive manufacturing technologies: Round robin study," *Additive Manufacturing*, vol. 36, pp. 1–24, article 101 564, Dec. 2020.

[19] O. C. Zienkiewicz, R. L. Taylor, and J. Z. Zhu, *The finite element method: Its basis and fundamentals*, 7th ed. Butterworth-Heinemann, Aug. 2013.

[20] M. S. Alnæs, J. Blechta, J. Hake, A. Johansson, B. Kehlet, A. Logg, C. Richardson, J. Ring, M. E. Rognes, and G. N. Wells, "The FEniCS Project version 1.5," *Archive of Numerical Software*, vol. 3, no. 100, pp. 9–23, Dec. 2015.